

Mid-infrared Extinction Spectra and Optical Constants of Supercooled Water Droplets

Robert Wagner,* Stefan Benz, Ottmar Möhler, Harald Saathoff, Martin Schnaiter, and Ulrich Schurath

Forschungszentrum Karlsruhe, Institute of Meteorology and Climate Research (IMK-AAF), Karlsruhe, Germany

Received: April 14, 2005; In Final Form: June 15, 2005

Complex refractive indices of supercooled liquid water have been retrieved at 269, 258, 252, and 238 K in the 4500–1100 cm^{-1} wavenumber regime from series of infrared extinction spectra of micron-sized water droplets. The spectra collection was recorded during expansion experiments in the large coolable aerosol chamber AIDA of Forschungszentrum Karlsruhe. A Mie inversion technique was applied to derive the low-temperature refractive index data sets by iteratively adjusting the room-temperature optical constants of liquid water until obtaining the best agreement between measured and calculated infrared spectra of the supercooled water droplets. The new optical constants, revealing significant temperature-induced spectral variations in comparison with the room-temperature refractive indices, proved to be in good agreement with data sets obtained in a recent study. A detailed analysis was performed to elaborate potential inaccuracies in the retrieval results when deriving optical constants from particle extinction spectra using an iterative procedure.

Introduction

The quantitative analysis of mid-infrared aerosol extinction spectra in terms of particle phase, composition, volume, and size distribution relies on accurate complex refractive indices for the various aerosol constituents. Literature data of temperature- and frequency-dependent optical constants, i.e., the real and imaginary parts of the complex refractive index, n and k , are comprehensively tabulated in the HITRAN database of spectroscopic parameters for a majority of important atmospheric aerosol species.^{1,2} Recent studies especially underlined the notable variations of the optical constants with temperature, e.g., the strong temperature dependence of the water ice spectrum³ in the O–H stretching regime at around 3250 cm^{-1} and the temperature-induced changes in the dissociation behavior of supercooled $\text{H}_2\text{SO}_4/\text{H}_2\text{O}$, $\text{HNO}_3/\text{H}_2\text{O}$, and $\text{H}_2\text{SO}_4/\text{H}_2\text{O}/\text{HNO}_3$ solution droplets,^{4–10} leading to a dramatic variation of the optical constants in the sulfate and nitrate absorption regime with temperature. However, there is one key compound whose low-temperature optical constants in the mid-infrared spectral region were unknown until most recently, namely, supercooled water. Before 2005, two studies reported refractive indices of water at temperatures below 273 K: Kou et al.¹¹ have measured the k spectrum of water at 265 K in the near-infrared at wavenumbers $>4000 \text{ cm}^{-1}$, whereas Zelsmann et al.¹² extracted optical constants from thin film spectra of water at 267 K in the far IR (450–25 cm^{-1}). In the mid-IR regime, covering the O–H stretching mode at about 3400 cm^{-1} and the H–O–H bending mode at around 1640 cm^{-1} , the influence of temperature on the optical constants was only analyzed down to a minimum temperature of 274 K.¹³ The results from Pinkley et al.¹³ indicate that the temperature decrease from 300 to 274 K already leads to a substantial change in the refractive indices of water, e.g., a more than 10% increase in the maximum of the absorption index k in the O–H stretching regime, accompanied by a slight frequency shift of 10 cm^{-1} toward lower wavenumbers, as well

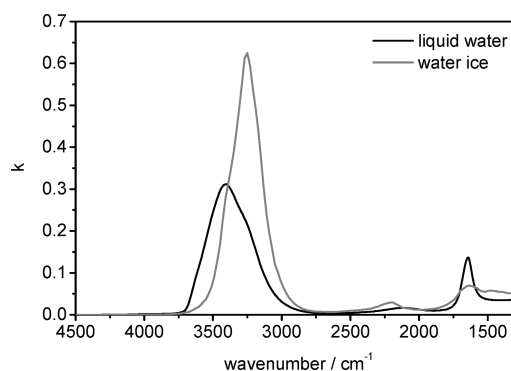


Figure 1. Comparison of the absorption indices of liquid water at 298 K¹⁴ and water ice at 266 K¹⁵ in the mid-infrared regime.

as a slight reduction of the peak intensity of the H–O–H bending mode. To assess these spectral variations in the absorption spectrum of water with temperature, Figure 1 depicts the k spectra of liquid water at room temperature (the recommended values from Bertie and Lan¹⁴) as well as water ice at 266 K (from the compilation of Warren¹⁵).

It is evident that the spectral trends observed by Pinkley et al.¹³ reflect a slight assimilation of the k spectrum of room-temperature water to the spectrum of ice upon cooling. One might expect that these variations (e.g., the intensity increase and low-frequency shift in the O–H stretching regime) will be even more pronounced in the spectrum of supercooled water droplets at temperatures between 273 K and the homogeneous nucleation temperature of about 236 K.

In a study published by the end of 2004, Zsatsky et al.¹⁶ clearly demonstrated that room-temperature optical constants of water indeed failed to accurately reproduce a measured spectrum of supercooled water droplets at 243 K in the 6000 to 450 cm^{-1} regime (see Figure 4 in their publication). A much better fit result was obtained for a combination of the liquid water (298 K) and water ice optical constants, indicating that the optical constants of supercooled water can roughly be

* Corresponding author. E-mail: Robert.Wagner@imk.fzk.de.

reproduced by co-adding a suitable fraction of ice refractive indices to the room-temperature optical constants of water. This fraction rises from about 0.02 for extinction spectra recorded at 300 K to 0.30 for highly supercooled water droplets at 240 K. In view of the results from complementary molecular dynamic simulations, this temperature-dependent change in the spectral signatures was ascribed to an increasing amount of crystal-like, low-density domains in supercooled water with decreasing temperature. In light of the spectroscopic results, the refractive indices of these domains, as a first approximation, can be represented by those of hexagonal ice. As already pointed out by Zasetsky et al.,¹⁶ these findings clearly demonstrate that care has to be taken when analyzing mixed phase clouds composed of supercooled water droplets and ice crystals in mid-infrared remote sensing applications; particularly when, for lack of accurate refractive indices of supercooled water, room-temperature optical constants of water are employed to represent absorption and scattering by supercooled water droplets.^{17,18} This may lead to retrieval errors with respect to the ratio of cloud liquid water to ice water content, taking into consideration that the actual refractive indices of supercooled water according to the Zasetsky et al.¹⁶ study are approximately a mixture of the optical constants of room-temperature water and ice.

In our present study, we adopted an iterative approach to extract mid-infrared optical constants of supercooled water from measured extinction spectra of supercooled water droplets. Just when preparing this manuscript, a succeeding work from Zasetsky et al.¹⁹ has been published, bringing up the identical subject. The authors have derived the first data sets of mid-infrared optical constants of supercooled water from aerosol extinction spectra in the 4000–460 cm^{-1} regime for four temperatures between 273 and 240 K. Their results nicely reveal that the k spectra of supercooled water indeed gradually adopt the spectral features of ice upon cooling. Undoubtedly, these new data sets will improve the accuracy by which mixed phase clouds composed of ice crystals and supercooled water droplets can be analyzed in terms of the relative volume concentrations of both species. Our own independent analysis, carried out at nearly the same time, is complementary to the work of Zasetsky et al.¹⁹ by providing a first stringent test of the new refractive index data sets. But furthermore, as we employed a different Mie inversion technique to derive the optical constants from the infrared spectra, our results will reveal more clearly the inaccuracies that might be introduced when applying an iterative approach to determine optical constants from aerosol extinction measurements. The present experiments were conducted in the large coolable aerosol chamber AIDA of Forschungszentrum Karlsruhe. As described in detail in our recent publications, the AIDA chamber may be operated as a moderate expansion chamber to study cloud formation over an extended temperature range from 273 to 193 K.^{20,21} From recent expansion experiments at temperatures between 270 and 235 K, we obtained series of infrared extinction spectra of micron-sized supercooled water droplets. As in the Zasetsky et al.^{16,19} studies, Mie fits using room-temperature optical constants of water poorly mimicked our measured spectra. Using a standard optimization technique, the room-temperature refractive indices from Bertie and Lan¹⁴ were iteratively adjusted by minimizing the summed squared residuals between measured and calculated infrared spectra. Thereby, we derived four discrete data sets of optical constants for supercooled water at 269, 258, 252, and 238 K in the 4500–1100 cm^{-1} spectral range. Independent measurements of cloud droplet diameters with an optical particle counter were

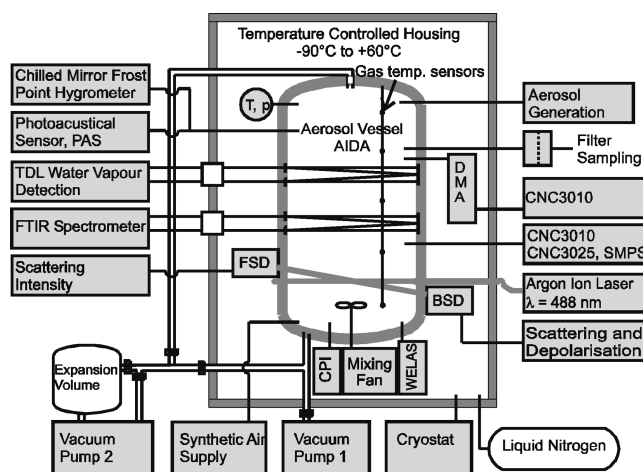


Figure 2. Schematic view of the AIDA chamber facility, showing the major instrumentation used in the expansion experiments. Scientific instruments as well as aerosol generation devices are located on four separate floors surrounding the isolating housing.

used to assess the accuracy of our iterative approach to derive the refractive index data sets.

Methods

A schematic cross section of the AIDA aerosol chamber facility, including the major scientific instrumentation used in this study, is shown in Figure 2.

The cylindrical aluminum aerosol vessel, volume 84 m^3 , is located inside a large isolating housing whose interior can be cooled to any temperature between ambient and 183 K. The temperature inhomogeneity throughout the entire vessel is less than ± 0.5 K. The chamber can be evacuated with two vacuum pumps from atmospheric pressure to a final pressure of about 0.01 hPa. Details about the cooling and vacuum systems, gas supply, as well as temperature and pressure measurements are described in our recent publications^{20,21} and are available on the AIDA web page, <http://imk-aida.fzk.de>. Most important instruments in the present study include the FTIR spectrometer, the optical particle counter (type WELAS, Palas, size range: 0.8–45 μm), and the commercial cloud particle imaging (CPI) system, offering a resolution of 2.3 μm .²² The FTIR spectrometer (type IFS 66v, Bruker) is located at medium height of the AIDA vessel. Using an internal White-type multiple reflection cell, infrared extinction spectra can be recorded in situ with optical path lengths of up to 250 m. The transmittance of the BaF_2 cell windows allows for measurements in the 800–6000 wavenumber range. Both the WELAS and CPI instruments are mounted in the cold housing below the aluminum vessel and both use vertical sampling tubes to minimize sampling losses (sampling flows: 5 L/min, WELAS; 200 L/min, CPI).

The following section will be divided into two subsections. In the first part, we will briefly review the operation of the AIDA vessel as a moderate expansion cloud chamber and describe two types of expansion experiments from which series of infrared extinction spectra of supercooled water droplets with diameters ranging from 2 to 11 μm were obtained. Our iterative approach to extract the optical constants of supercooled water from these infrared spectra series will be presented in the second part.

AIDA Expansion Experiments. Previous AIDA expansion experiments have proven to be successful in studying the ice nucleation potential of a variety of atmospheric aerosols such as $\text{H}_2\text{SO}_4/\text{H}_2\text{O}$ solution droplets,²¹ soot, and mineral dust

particles,²³ as well as internally mixed aerosol particles (e.g., soot coated with sulfuric acid²⁰) in the 233–193 K temperature range.

A typical ice nucleation experiment involves the following steps: (i) Cleaning of the aerosol vessel by evacuating the chamber to <0.01 hPa and performing several flushing cycles with particle-free synthetic air. Background aerosol number concentrations are typically below 0.1 cm^{-3} after refilling the evacuated chamber with synthetic air to 1000 hPa. (ii) Coating of the aluminum walls of the aerosol vessel with a thin ice layer, made by filling the chamber with humidified air at some higher temperature and subsequent cooling to a lower temperature, chosen as the initial temperature for the expansion experiment. This ensures that expansion cooling experiments are started at an ice saturation ratio $S_{\text{ice}}(T)$ close to unity, where $S_{\text{ice}}(T)$ is defined as the ratio of the actual water vapor pressure $p_w(T)$ and the saturation water vapor pressure over ice $p_{w,\text{ice}}(T)$ at the same temperature. (iii) Addition of the desired seed aerosol, with number concentrations typically ranging from 10 to 1000 cm^{-3} , and subsequent aerosol characterization by, e.g., filter sampling and size distribution measurements (Figure 2). (iv) Start of the expansion cooling to initiate ice nucleation by establishing large supersaturations with respect to the ice phase. Typically, the AIDA pressure is reduced from 1000 to 800 hPa within 4–10 min (depending on the pumping speed of the mechanical pump). At slow pumping speeds, cooling rates as low as 0.1 K min^{-1} can be controlled; the maximum pumping speed, in contrast, leads to a cooling rate of initially more than 4 K min^{-1} . During pumping, $p_{w,\text{ice}}$ exponentially decreases with decreasing AIDA gas temperature whereas p_w decreases at most linearly with the total pressure. As a consequence, ice saturation ratios >1.6 can be established in the course of the expansion cooling. Ice nucleation occurs upon exceeding a critical threshold relative humidity, its magnitude critically dependent on the nature of the seed aerosol and the temperature. The onset of ice nucleation can be detected using a variety of independent diagnostic techniques (Figure 2): (i) Increase in depolarization of backscattered laser light, (ii) detection of large ice crystals with the WELAS optical particle counter, (iii) imaging of nucleated ice crystals with the CPI system, (iv) appearance of the characteristic extinction features of ice in the infrared spectra. Complementarily, p_w is measured in situ by tunable diode laser absorption spectroscopy with a time resolution of 1 s, thus allowing for a direct determination of the critical ice saturation ratio at the onset of ice formation.

Recent studies addressed the efficiency of mineral dust particles as water and ice cloud nuclei at temperatures between 273 and 250 K as well as the homogeneous freezing of almost pure, micron-sized supercooled water droplets at around 236 K, generated by liquid activation of $\text{H}_2\text{SO}_4/\text{H}_2\text{O}$ solution droplets during an AIDA expansion experiment. Both types of experiments, although primarily dedicated to our ongoing interest in the ice nucleating ability of aerosol particles, also proved to be adequate to acquire series of mid-infrared extinction spectra of supercooled water droplets.

Expansion Cooling Experiment with Mineral Dust Particles. At temperatures between 273 and 250 K, ice formation on mineral dust particles during AIDA expansion experiments may proceed in two ways. Once the chamber air is supersaturated with respect to ice, deposition nucleation, i.e., direct growth of ice on the mineral dust surface by vapor deposition, may occur. Alternatively, the mineral dust particles can act as cloud condensation nuclei once water saturation is surpassed, followed

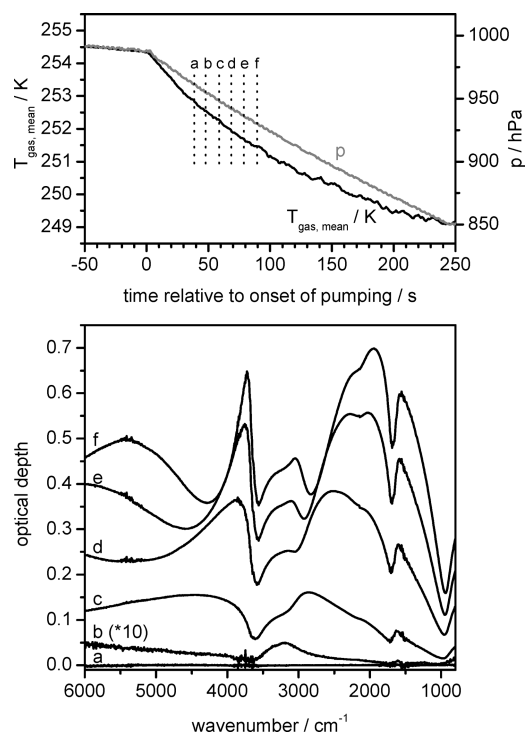


Figure 3. AIDA expansion experiment with redispersed Sahara dust aerosol particles acting as cloud condensation nuclei. Top: time profiles of total pressure and mean gas temperature during the expansion. Time zero denotes the start of pumping. Note that pressure and temperature are already decreasing, albeit much more slowly, before the mechanical pump was started at $t = 0$ s. This is due to the large sampling rates of the optical particle counters. Dotted vertical lines indicate the time when individual FTIR extinction spectra were recorded in course of the expansion. The spectra are shown in the bottom panel; spectrum b was upscaled by a factor of 10.

by immersion freezing of the cloud droplets at a sufficiently low temperature. However, depending on temperature and the specific ice nucleating ability of the mineral dust samples, deposition nucleation and/or immersion freezing may also fail to appear. Exactly from such expansion cooling experiments with the absence of ice formation, as exemplarily shown in Figure 3, infrared spectra series of supercooled water droplets were obtained.

In the experiment presented in Figure 3, dry redispersed dust aerosol particles from the Sahara desert region were used as seed aerosol. The expansion was started at $T = 254.5 \text{ K}$ and at an ice saturation ratio of about 0.98 (corresponding to a saturation ratio with respect to liquid water of about 0.82). After the start of pumping, FTIR extinction spectra were recorded in time intervals of 10 s at a resolution of 4 cm^{-1} by co-adding 40 scans. As a consequence of its low number concentration (200 cm^{-3}), the spectral signatures of the dust aerosol are not visible in the infrared spectra, cf. Figure 3 (lower panel, trace a). Extinction features of a liquid water cloud became apparent about 45 s after the start of the expansion, i.e., when 100% relative humidity with respect to supercooled water was exceeded (spectrum b). The FTIR spectra series nicely reveals the continuous growth of the cloud droplets. Spectra d–f bare a pronounced Mie interference structure at nonabsorbing wavenumbers $>4000 \text{ cm}^{-1}$, indicating a very narrow size distribution of the water droplets.²⁴ The simultaneous measurements with the CPI system provided evidence that ice was formed neither by deposition nucleation nor by immersion freezing in this particular experiment. Note that ice particles can be clearly identified with the CPI because they immediately grow to much

larger sizes than the supercooled droplets owing to the high ice supersaturation in their presence. Thereby the imaging system is sensitive to ice particle number concentrations as low as 0.01 cm^{-3} . Hence, the series of five extinction spectra of growing water droplets (spectra b–f) from this AIDA expansion was used to extract mid-infrared optical constants of supercooled water at $T = 252 \text{ K}$ (i.e., the mean temperature over the time period of recording the five spectra). From similar expansion experiments with the absence of ice formation, two further spectra series of supercooled water droplets were obtained at $T = 256$ and 260 K . The extinction spectra from both expansions were used to derive an averaged refractive index data set for supercooled water at 258 K . As opposed to these purposely selected AIDA expansion experiments, which only resulted in liquid activation of the seed aerosol without freezing, other types of mineral dust, e.g., from different regions of the Sahara desert or samples from desert regions in Asia, proved to be efficient deposition and immersion freezing ice nuclei, especially at temperatures below about 253 K . The detailed analysis of the ice nucleating ability of various types of mineral dust aerosol will be presented in a manuscript currently in preparation.

As noted above, expansion experiments with mineral dust particles as seed aerosol were also started at initial gas temperatures being as high as 273 K . However, as will be justified in the next section, different AIDA expansion experiments, addressing the efficiency of environmental bacteria (*Pseudomonas syringae*) as ice nuclei at $T = 270\text{--}265 \text{ K}$, were used to retrieve an additional refractive index data set for supercooled water at these higher temperatures. Specifically, an infrared spectra series of water droplets recorded during an AIDA expansion experiment at 269 K with environmental bacteria as seed aerosol (bacteria mixed with a small amount of residual aerosol particles after wet dispersion of the bacterial suspension), not acting as ice nuclei under our experimental conditions, was used to retrieve this data set.

Strictly speaking, we do not generate pure water droplets in the course of the AIDA expansion experiments. Instead, the pre-added seed aerosol particles are embedded in the supercooled water droplets after the liquid activation. Hence, we have to check that the presence of these small inclusions does not significantly alter the extinction spectra of micron-sized water droplets compared to pure water spectra. For this purpose, we have made the following test calculations, addressing the experiments with mineral dust particles as cloud condensation nuclei: As a reference, we have calculated frequency-dependent extinction cross sections of log-normally distributed water droplets with a count median diameter of $5 \mu\text{m}$ and a mode width of 1.3 using the optical constants of Bertie and Lan.¹⁴ Thereafter, we have recalculated the reference spectrum with all droplets containing a monodisperse spherical dust inclusion of $0.5 \mu\text{m}$, which is the typical median diameter of the redispersed mineral dust samples employed in our studies. The dust inclusion simply replaces an equivalent volume fraction of liquid water in the droplets, thus leaving the overall particle diameters unchanged. The extinction spectrum of the composite particles was calculated using the coated sphere subroutine provided by Bohren and Huffman,²⁴ extended to average over log-normally distributed particle sizes. The dust inclusion was mimicked as internal mixture of 10 vol % hematite and 90 vol % quartz. The corresponding optical constants were obtained from the HITRAN database (refractive index data tabulated by E. P. Shettle).^{1,2} The calculated extinction spectra of water droplets with and without dust inclusion are compared in Figure 4, panels a and b. Obviously, the dust inclusion leaves the water

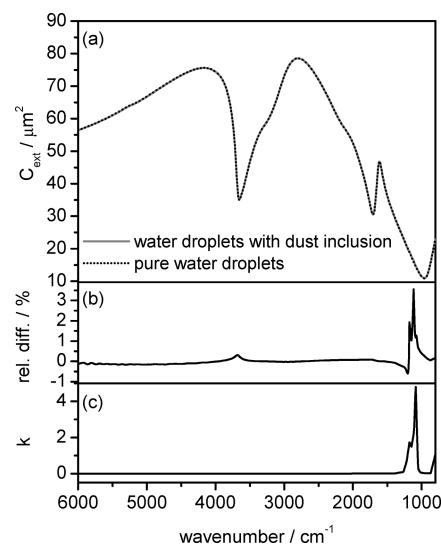


Figure 4. (a) Calculated extinction cross sections (C_{ext}), (i) for pure, log-normally distributed water droplets (count median diameter $5 \mu\text{m}$, mode width 1.3) and (ii) for a cloud of water droplets with identical overall size distribution parameters, but all droplets containing a monodisperse spherical dust inclusion of $0.5 \mu\text{m}$ in diameter. The percentage difference between spectra (ii) and (i), shown in panel b, is compared with the absorption index (k) spectrum of the dust inclusion, employed for calculating the extinction features of the composite particles with the coated sphere approach (panel c).

extinction features virtually unaffected. Marginal spectral deviations can be seen at about 1100 cm^{-1} . Here, the intense silicate absorption band of quartz (see Figure 4, panel c) leads to a slight increase in extinction in the composite particles compared to the pure water droplets. Nonetheless, the calculations clearly reveal that the extinction spectra of water droplets, obtained from AIDA expansion experiments with dust particles as seed aerosol, can be treated as pure droplet spectra in our subsequent analysis to derive the optical constants of supercooled water. We expect the same to be true for the expansion experiment with the environmental bacteria as cloud condensation nuclei, having a similar median diameter as the dust aerosol particles.

Expansion Cooling Experiment with Supercooled $\text{H}_2\text{SO}_4/\text{H}_2\text{O}$ Solution Droplets. In addition to the infrared spectra series of supercooled water droplets at $T = 269, 258,$ and 252 K , another set of FTIR extinction spectra was obtained close to the homogeneous nucleation temperature of pure water droplets from an AIDA expansion experiment with supercooled sulfuric acid solution droplets as seed aerosol (number concentration $\sim 250 \text{ cm}^{-3}$, median droplet diameter $\sim 0.3 \mu\text{m}$, initial composition $\sim 31 \text{ wt } \%$ H_2SO_4 at 70% relative humidity). The expansion was started at $T = 243 \text{ K}$, and the time profiles of total pressure and mean gas temperature as well as selected FTIR extinction spectra recorded during the expansion experiment are shown in Figure 5. As the optical path length of the White cell was reduced to avoid saturation of the infrared spectrum when a cloud of large droplets and/or ice crystals is formed during the expansion, the spectral features of the small amount of pre-added sulfuric acid droplets remain below our detection limit. For the same reason, the initial dilution of the $\text{H}_2\text{SO}_4/\text{H}_2\text{O}$ droplets (“haze formation”) upon start of expansion cooling, driven by the increasing relative humidity, is not detectable. However, once water saturation is surpassed, the activated $\text{H}_2\text{SO}_4/\text{H}_2\text{O}$ aerosol particles rapidly grow to micron-sized cloud droplets, as can be nicely seen in the series of FTIR extinction measurements (spectra a–e).

In the later course of the expansion experiment, the mean gas temperature gradually approaches and eventually falls below

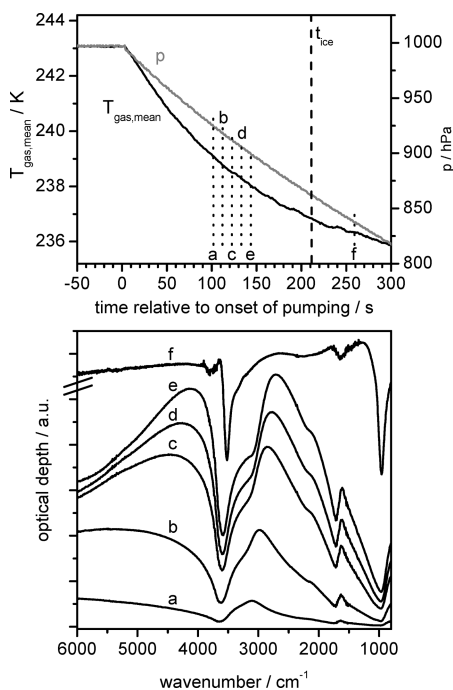


Figure 5. AIDA expansion experiment with supercooled $\text{H}_2\text{SO}_4/\text{H}_2\text{O}$ solution droplets as seed aerosol. Top: time profiles of total pressure and mean gas temperature during the expansion. Dotted vertical lines indicate the time when individual FTIR extinction spectra were recorded in course of the expansion. The corresponding spectra are shown in the bottom panel; spectrum f was offset for clarity. The dashed vertical line in the top figure marks the freezing onset of the cloud droplets, afore generated by liquid activation of the sulfuric acid droplets.

the homogeneous ice nucleation temperature for supercooled water droplets. At about 210 s after the start of pumping, our ice-detecting diagnostics indicate the onset of freezing of the cloud droplets. An exemplary FTIR extinction spectrum after ice formation is shown in Figure 5 (spectrum f), clearly revealing the characteristic extinction minima (Christiansen bands) of large ice crystals at around 3500 and 950 cm^{-1} .²⁵ The analysis of this expansion experiment in terms of water freezing and homogeneous nucleation rates will be addressed in a future report. As for the present study, the set of droplet extinction spectra a–e was used for the derivation of infrared optical constants of supercooled water at $T \sim 238$ K. As will be shown in a later section, the median diameters of the water droplets are in the range 2.2–5.9 μm , corresponding to residual sulfuric acid weight fractions in the range 0.08–0.004 wt %. This insignificant amount of H_2SO_4 will be neglected in the subsequent analysis; i.e., measurements a–e will be treated as pure water extinction spectra.

Iterative Approach To Derive the Optical Constants of Supercooled Water. The derivation of the real and imaginary parts of the complex refractive index $N(\tilde{\nu}) = n(\tilde{\nu}) + ik(\tilde{\nu})$ from transmission spectra exploits the Kramers–Kronig transform,²⁴ relating n and k according to

$$n(\tilde{\nu}_0) - 1 = \frac{2}{\pi} P \int_0^{\infty} \frac{k(\tilde{\nu}) \tilde{\nu}}{\tilde{\nu}^2 - \tilde{\nu}_0^2} d\tilde{\nu} \quad (1)$$

As the imaginary part k is directly proportional to the absorption coefficient for light propagation in a homogeneous bulk sample, the complete k spectrum can be, in principle, accurately retrieved from, e.g., thin-film absorption measurements, provided that reflections occurring at the sample interfaces are properly

accounted for.²⁶ The subsequent Kramers–Kronig integration then yields the corresponding n spectrum. When dealing with particle extinction spectra as in our present study, a straightforward approach to extract the optical constants is only feasible given that the particle diameter is small enough that the extinction cross section C_{ext} approximately equals the Rayleigh absorption cross section $C_{\text{abs}}^{\text{Rayl}}$. For transmission measurements in air, $C_{\text{abs}}^{\text{Rayl}}$ is given by

$$C_{\text{abs}}^{\text{Rayl}} = \frac{6\pi V \text{Im} \frac{N^2 - 1}{N^2 + 2}}{\lambda} \quad (2)$$

where V denotes the particle volume.²⁴ Taking into account that also the real and imaginary parts of the composite function f ,

$$f = \frac{N^2 - 1}{N^2 + 2} \quad (3)$$

whose imaginary part appears in eq 2, are related through a Kramers–Kronig transform,²⁷ the optical constants may be derived from small-particle absorption spectra given that the particle volume is known. Applying this methodology to extract the mid-infrared optical constants from transmission spectra of supercooled water droplets, however, requires droplet diameters below about 0.2 μm to fulfill the condition that $C_{\text{ext}} \cong C_{\text{abs}}^{\text{Rayl}}$. Water droplets of that size cannot be made and maintained in a chamber experiment. Hence, a different strategy has to be devised for the analysis of our extinction spectra of micron-sized water droplets obtained from the AIDA expansion experiments. In the following, we will outline an iterative approach whose underlying idea consists of a stepwise adjustment of the room-temperature optical constants of water to minimize the summed squared residuals of Mie fits to our measured infrared spectra of supercooled water droplets. The procedure, inspired by several similar Mie inversion techniques described in the literature,^{28–30} involves the following steps:

(i) A series of typically five infrared extinction spectra of growing water droplets provides the basis for the derivation of the optical constants. The recorded optical depth is proportional to the aerosol number density N , the size-averaged extinction cross section $\langle C_{\text{ext}} \rangle$, and the optical path length L . All spectra recorded during an expansion experiment were normalized to give equal weight to each individual spectrum in the subsequent analysis. Spectra calculated from Mie theory were then fitted to the measured FTIR extinction spectra, using the room-temperature optical constants of water from Bertie and Lan¹⁴ as input values and assuming log-normally distributed particle sizes,

$$\langle C_{\text{ext}} \rangle = \int_{D_{p,\text{min}}}^{D_{p,\text{max}}} C_{\text{ext}}(D_p) \phi(D_p) dD_p \quad \phi(D_p) = \frac{1}{\sqrt{2\pi} D_p \ln \sigma_g} \exp \left\{ -\frac{(\ln D_p - \ln \text{CMD})^2}{2(\ln \sigma_g)^2} \right\} \quad (4)$$

with $\phi(D_p) dD_p$ denoting the fraction of particles per unit volume having particle diameters between D_p and $D_p + dD_p$. The droplet number concentration N as well as the count median diameter CMD and the mode width σ_g of the log-normal size distribution were retrieved by minimizing the summed squared residuals between measured and calculated spectra, using the downhill simplex algorithm as the optimization technique.^{31,32} Thereby,

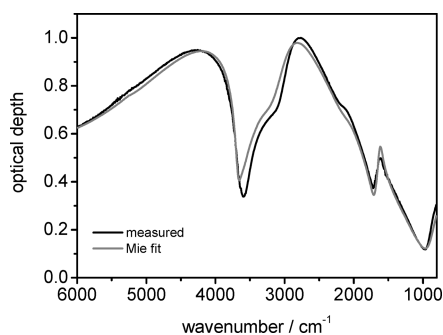


Figure 6. Comparison between a measured extinction spectrum of supercooled water droplets at 238 K (trace d in Figure 5) and a Mie fit using the room-temperature optical constants of water from Bertie and Lan¹⁴ as input. The droplet parameters retrieved in step (i) are $N_4 = 235 \text{ cm}^{-3}$, $\sigma_{g,4} = 1.20$, $\text{CMD}_4 = 5.32 \text{ }\mu\text{m}$.

we obtained an initial set of size distribution parameters for each spectrum:

$$\begin{array}{llll}
 \text{spectrum 1:} & N_1 & \sigma_{g,1} & \text{CMD}_1 \\
 \text{spectrum 2:} & N_2 & \sigma_{g,2} & \text{CMD}_2 \\
 \text{spectrum 3:} & N_3 & \sigma_{g,3} & \text{CMD}_3 \\
 \text{spectrum 4:} & N_4 & \sigma_{g,4} & \text{CMD}_4 \\
 \text{spectrum 5:} & N_5 & \sigma_{g,5} & \text{CMD}_5
 \end{array} \quad (5)$$

An exemplary Mie fit result is presented in Figure 6, revealing that the room-temperature data only poorly reproduce our measured extinction spectrum of supercooled water droplets. As a quantitative measure for the performance of the optical constants, the summed squared residuals of all individual Mie fits were co-added. In the next step, this quantity was minimized by adjusting the optical constants employed in the Mie calculations.

(ii) In this minimization process, we used the complete spectrum of the imaginary index k from 6000 to 800 wavenumbers as optimization parameters, corresponding to 675 grid points when limiting the spectral resolution to 8 cm^{-1} . This proved to be sufficient to resolve the broad-band extinction features of our droplet spectra. Again, the downhill simplex method was employed as the optimization technique.³³ The k spectrum from Bertie and Lan¹⁴ was used as starting point. Once the algorithm proposed a new k spectrum, the corresponding n spectrum was calculated via Kramers–Kronig transformation, as will be described in detail in a separate paragraph below. With this new set of n and k , we recalculated the droplet extinction spectra using the size distribution parameters obtained in step (i), thereby obtaining a new value for the sum of all residuals between measured and calculated infrared spectra. Depending on its magnitude, the newly proposed k spectrum either was rejected by the optimization algorithm or was used as starting point for a new iteration. Typically, up to 10 000 iterations were performed in this step. To avoid the occurrence of singular spikes, newly proposed k spectra were subjected to a weak smoothing function prior to the Kramers–Kronig transformation (Savitzky–Golay smoothing filter, quadratic polynomial fit, 5 points in the moving window³³).

(iii) In step (ii), the room-temperature optical constants of water were fine-tuned by improving the quality of the Mie fits to our measured spectra of supercooled water droplets. The Mie calculations, however, still relied on size distribution parameters that were obtained from Mie fits using the original Bertie and Lan¹⁴ data. Therefore, after about 10 000 iterations, the Mie fits of step (i) were repeated with the modified set of optical

constants to attain a corrected set of size distribution parameters, marked by asterisks,

$$\begin{array}{llll}
 \text{spectrum 1:} & N^*_1 & \sigma^*_{g,1} & \text{CMD}^*_1 \\
 \text{spectrum 2:} & N^*_2 & \sigma^*_{g,2} & \text{CMD}^*_2 \\
 \text{spectrum 3:} & N^*_3 & \sigma^*_{g,3} & \text{CMD}^*_3 \\
 \text{spectrum 4:} & N^*_4 & \sigma^*_{g,4} & \text{CMD}^*_4 \\
 \text{spectrum 5:} & N^*_5 & \sigma^*_{g,5} & \text{CMD}^*_5
 \end{array} \quad (6)$$

which in turn was used to reiterate step (ii). Steps (i) and (ii) were then alternately repeated until the spectral changes in the optical constants after step (ii) had become so small that the newly derived size distribution parameters differed by less than 0.1% from the values of the previous iteration step.

As an important advantage of the AIDA expansion experiments, our iterative approach to extract the optical constants relies on a series of extinction spectra of variably sized water droplets, all of them exhibiting varying fractional amounts of light scattering and light absorption. This provides for a unique retrieval result in terms of the optical constants, because our newly derived n and k data are simultaneously applied to all, equally weighted individual spectra. In contrast, with only one droplet extinction spectrum at hand, there might be some trade off between the optical constants and the size distribution parameters, leading to a nonunique fit result. However, it proved to be necessary to include at least two droplet spectra corresponding to median diameters of $\leq 6 \text{ }\mu\text{m}$ in the fit algorithm to obtain a consistent fit result for the spectrum of the imaginary index k . Larger droplet spectra, as being increasingly dominated by light scattering, are less sensitive to small changes in the k spectrum, e.g., in the regime of the O–H stretching mode. The size of the cloud droplets generated in the course of the AIDA expansion experiments depends on the seed aerosol number concentration as well as the prevailing water vapor concentration, which, due to the ice-covered chamber walls, exponentially increases with increasing temperature. For temperatures $> 265 \text{ K}$ and seed aerosol number concentrations $< 300 \text{ cm}^{-3}$, the generated water droplets rapidly grow to diameters $> 10 \text{ }\mu\text{m}$ within the time frame of only two successive FTIR extinction measurements. Under such conditions, being representative for the expansion experiments with mineral dust particles as seed aerosol at $T > 265 \text{ K}$, the recorded FTIR spectra series does not provide a suitable basis for a unique retrieval of the refractive indices. Exactly for this reason, we used the AIDA expansion experiment with environmental bacteria as cloud condensation nuclei to retrieve the refractive index data set for supercooled water at 269 K. Here, a higher seed aerosol number concentration was provided, thus resulting in a high number concentration of comparatively small cloud droplets during the activation, having a maximum diameter of $< 6 \text{ }\mu\text{m}$.

Kramers–Kronig Transformation. As an essential step in our iterative approach to derive the optical constants of supercooled water, the Kramers–Kronig transformation is applied to calculate the n spectrum from a new guess for the spectrum of the imaginary index k . As inherent in eq 1, this integration requires that k is known over the complete wavenumber range and not only over a finite region from 6000 to 800 cm^{-1} , the experimentally accessible wavenumber regime of our present study. Therefore, it is essential to expand the k spectrum to wavenumbers beyond the regime covered by the actual measurements. Many studies have demonstrated that the inaccuracies, which are introduced by the extension of the wavenumber regime, are significantly reduced by employing the so-called subtractive Kramers–Kronig relation.^{3,28,34,35} Here,

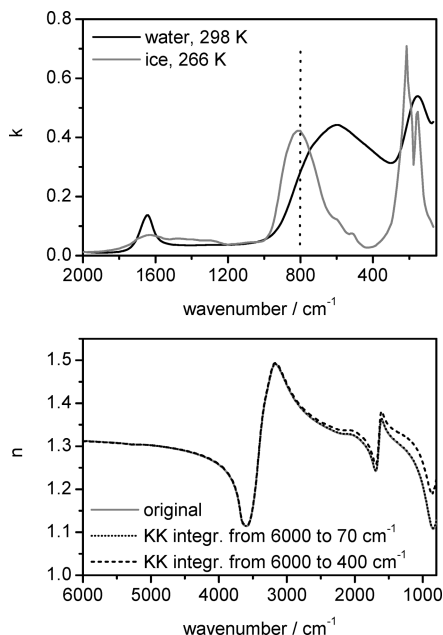


Figure 7. Top panel: the k spectra of liquid water and ice in the 2000–70 wavenumber range. A dashed vertical line indicates the low-frequency cutoff of the BaF₂ windows integrated in our White cell setup. Bottom panel: comparison of the original n spectrum of liquid water from Bertie and Lan¹⁴ from 6000 to 800 cm⁻¹ with the n spectra obtained from subtractive Kramers–Kronig transformations of the Bertie and Lan¹⁴ k spectrum in the 6000–70 and 6000–400 cm⁻¹ ranges.

the real part of the refractive index has to be known at some anchor point $\tilde{\nu}_x$ within the accessible wavenumber range:

$$n(\tilde{\nu}_x) - 1 = \frac{2}{\pi} P \int_0^{\infty} \frac{k(\tilde{\nu})\tilde{\nu}}{\tilde{\nu}^2 - \tilde{\nu}_x^2} d\tilde{\nu} \quad (7)$$

Subtracting eq 7 from eq 1 then yields the subtractive Kramers–Kronig expression to calculate n at any given wavenumber $\tilde{\nu}_0$:

$$n(\tilde{\nu}_0) = n(\tilde{\nu}_x) + \frac{2(\tilde{\nu}_0^2 - \tilde{\nu}_x^2)}{\pi} P \int_0^{\infty} \frac{k(\tilde{\nu})\tilde{\nu}}{(\tilde{\nu}^2 - \tilde{\nu}_0^2)(\tilde{\nu}^2 - \tilde{\nu}_x^2)} d\tilde{\nu} \quad (8)$$

As $n(\tilde{\nu}_0)$ is now determined in relation to the anchor point value $n(\tilde{\nu}_x)$, the errors introduced by an imprecise extrapolation of the k spectrum can be considerably reduced.

Despite the better performance of the subtractive Kramers–Kronig transformation, the extension of the k spectrum remains a crucial issue in our present application. As demonstrated by the top panel of Figure 7, showing the k spectra of room-temperature water and ice in the 2000–70 wavenumber range, our low-frequency cutoff of 800 cm⁻¹ just cuts the intense intermolecular rotational modes of water and ice,²⁴ centered at about 600 and 800 cm⁻¹, respectively. Further dominant absorption features, corresponding to intermolecular translational motions,²⁴ are located at wavenumbers below 400 cm⁻¹. To assess the importance of these low-frequency absorption bands in the Kramers–Kronig transformation, the lower panel of Figure 7 compares the original n spectrum of water from Bertie and Lan¹⁴ with the results from two different subtractive Kramers–Kronig integrations. In both calculations, the Bertie and Lan¹⁴ k spectrum was used for the integration, the anchor point was set to 5000 cm⁻¹ with $n = 1.3023$; in case (i) the k spectrum was limited to the 6000–400 cm⁻¹ range, in case (ii) to 6000–70 cm⁻¹. To perform the numerical integration, we

made use of the Maclaurin’s formula method as described by Ohta and Ishida.³⁶ As evidenced by the comparison, the k spectrum of water has to be extended to include both the intermolecular rotational and translational modes to properly reproduce the spectrum of the real refractive index in the 6000–800 wavenumber regime via the subtractive Kramers–Kronig analysis.

Hence, once the downhill simplex optimization algorithm proposes a new k spectrum for supercooled water in the 6000–800 wavenumber regime during step (ii) of our iterative approach, we have to extend the spectrum down to 70 cm⁻¹ to properly account for the low-frequency absorption bands of water in the subsequent Kramers–Kronig analysis. To estimate the shape of the k spectrum of supercooled water in the 800–70 wavenumber regime, we remember the results of Zsatsky et al.,¹⁶ noting that the infrared spectra of supercooled water droplets can roughly be reproduced by co-adding the refractive indices of warm water and ice. Thus, we apply a simple mixing rule to analyze a newly proposed k spectrum (k_{new}) by co-adding fractional amounts of the k spectra from Bertie and Lan¹⁴ as well as Warren:¹⁵

$$k_{\text{new}} = a k_{\text{water}} + (1 - a) k_{\text{ice}} \quad (9)$$

The mixing factor a , which best reproduced k_{new} in the 6000–800 cm⁻¹ regime, i.e., in our experimentally accessible wavenumber range, was used to calculate the spectrum of the imaginary index below the low-frequency cutoff of the BaF₂ windows, i.e., at wavenumbers from 800 to 70 cm⁻¹. Thereafter, this low-frequency k spectrum was properly scaled to match k_{new} at 800 cm⁻¹ and the subtractive Kramers–Kronig transformation was performed. Using the Lorentz–Lorenz relation,

$$\frac{n^2 - 1}{n^2 + 2} = \text{const} \cdot \rho_{\text{H}_2\text{O}} \quad (10)$$

the room-temperature anchor point value, $n(5000 \text{ cm}^{-1}) = 1.3023$, from the Bertie and Lan¹⁴ data set was adjusted to account for the actual AIDA temperature, using temperature-dependent densities of supercooled water ($\rho_{\text{H}_2\text{O}}$) measured by Hare and Sorensen³⁷ as input.

Not surprisingly, eq 9 proved to be only a crude approximation to describe our retrieved k spectra of supercooled water droplets. For example, the percentage deviations in the peak absorption of the O–H stretching mode can be as large as 20%. Hence, the same degree of uncertainty may be introduced into the spectral habitus of the low-frequency k spectrum, calculated using the simple mixing rule. To estimate the effect of these inaccuracies in the expanded k spectrum on the results of the Kramers–Kronig transformation, we have made some test calculations as follows: We combined our newly derived k spectrum for supercooled water at 252 K from 6000 to 800 cm⁻¹ with three different low-frequency expansions, thus mimicking some degree of uncertainty about the actual spectral habitus in this wavenumber regime. In the first place, we used the mixing factor a which best reproduced the 6000–800 cm⁻¹ spectrum ($a = 0.73$) to calculate k from 800 to 70 wavenumbers using eq 9. Two further low-frequency extensions were calculated using mixing factors of 0.65 and 0.81. The three different k spectra are shown in the top panel of Figure 8.

The spectral deviations in the 800–70 cm⁻¹ regime, being, e.g., as large as 25% for the intermolecular rotational mode, should be representative for the maximum inaccuracies that might be introduced by mimicking the k spectrum of supercooled

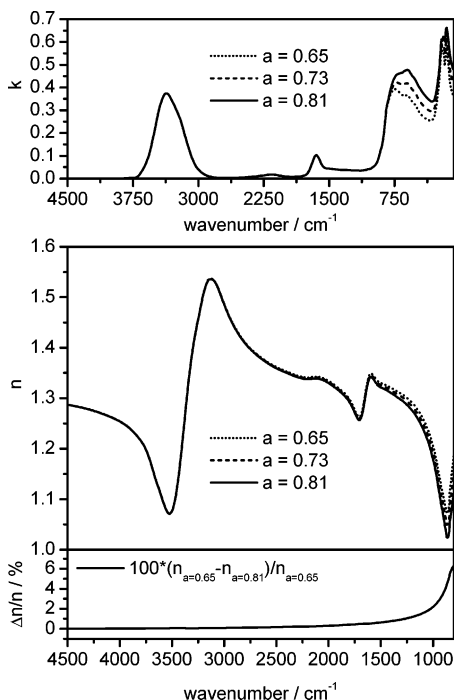


Figure 8. Top panel: A newly derived k spectrum for supercooled water at 252 K with three different low-frequency ($800\text{--}70\text{ cm}^{-1}$) extensions, calculated using eq 9 with mixing factors of $a = 0.65, 0.73,$ and 0.81 . Note that the $800\text{--}70\text{ cm}^{-1}$ spectra were scaled to fit the $6000\text{--}800\text{ cm}^{-1}$ k spectrum at 800 cm^{-1} . Bottom panel: spectra of the real refractive index n obtained from the subtractive Kramers–Kronig transformation of the three k spectra shown above. The attached panel shows the relative deviation of the n spectra corresponding to $a = 0.65$ and 0.81 . Below about 1100 cm^{-1} , this percentage error starts to exceed 2%.

water with the mixing rule (eq 9) in this wavenumber region. The n spectra, obtained from the subtractive Kramers–Kronig transformation of the three different k spectra, are shown in the bottom panel of Figure 8. Obviously, the various low-frequency extensions in the k spectrum hardly affect the Kramers–Kronig results for wavenumbers $>2000\text{ cm}^{-1}$. First, weak spectral variations between the different n spectra can be made out in the dispersion regime around 1600 cm^{-1} , the percentage error, however, still being as low as 0.5%. Only below 1100 cm^{-1} , the relative difference between the n spectra corresponding to $a = 0.65$ and 0.81 , $\Delta n/n$, starts to exceed 2%, thereafter rapidly increasing to about 6% at 800 cm^{-1} . Hence, we will restrict our data sets of optical constants to wavenumbers $>1100\text{ cm}^{-1}$ as a result of the uncertain spectral habitus of the low-frequency absorption bands of supercooled water beyond the 800 cm^{-1} cutoff of our infrared measurements.

At wavenumbers between 6000 and 4000 cm^{-1} , the absorption indices of water are generally very low, exhibiting only a weak absorption band at around 5150 cm^{-1} . Although our retrieved k data sets for supercooled water indeed show enhanced absorption in the $5200\text{--}5000\text{ cm}^{-1}$ regime (Figure 9), the applied iterative approach is not sensitive enough to accurately reproduce this absorption band, as can be seen by the strong scatter of our data in this frequency range. Hence, we propose to extend our k spectra beyond 4500 cm^{-1} with the near-infrared optical constants of supercooled water ($T = 265\text{ K}$) from Kou et al.¹¹

Results and Discussion

In the first part of this section, we will present our newly derived refractive index data sets for supercooled water at $T =$

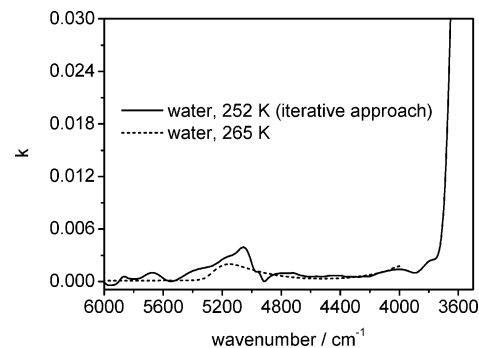


Figure 9. Newly derived k spectrum for supercooled water at 252 K in comparison with the k spectrum from Kou et al.¹¹ (supercooled water at 265 K) in the $6000\text{--}3500\text{ cm}^{-1}$ regime.

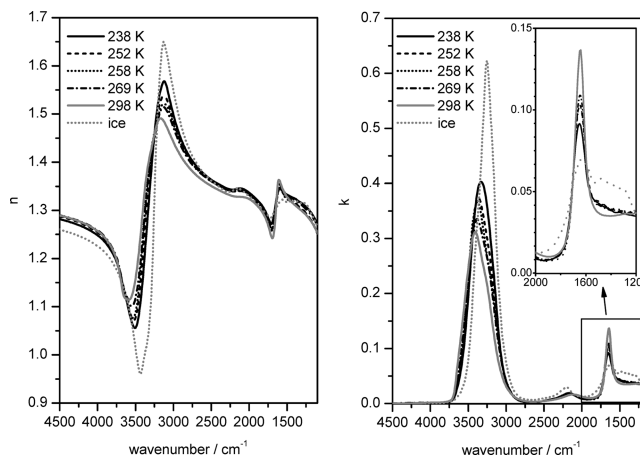


Figure 10. Real and imaginary parts of the complex refractive index for supercooled water at four temperatures between 269 and 238 K (black lines), as retrieved from our measured infrared extinction spectra. The room-temperature optical constants for water from Bertie and Lan¹⁴ (gray solid lines) as well as the water ice refractive indices from Warren¹⁵ (gray dotted lines) are shown for comparison.

269, 258, 252, and 238 K, demonstrate the improved quality of Mie fits to our measured extinction spectra compared to Mie calculations using the room-temperature optical constants of water, and compare retrieved droplet diameters with those simultaneously measured with the WELAS optical particle spectrometer. The second part is dedicated to a thorough comparison of the present data sets with those recently derived by Zsetsky et al.¹⁹

Figure 10 compares our retrieved n and k spectra for supercooled water with the room-temperature data from Bertie and Lan¹⁴ in the $4500\text{--}1100\text{ cm}^{-1}$ regime. Also shown are the water ice (266 K) optical constants from the compilation of Warren.¹⁵ Substantial temperature-induced changes in the absorption index spectra can be made out in both the regime of the O–H stretching mode and the H–O–H bending mode. The position of the O–H stretching band is gradually shifting to lower wavenumbers, i.e., from about 3405 cm^{-1} at 298 K toward 3300 cm^{-1} at the lowest temperature (238 K), thus approaching the frequency of the respective absorption band of ice, located at 3250 cm^{-1} . Accompanying this band shift, the maximum of the absorption index k increases by about 30% from 0.31 at 298 K to 0.40 at 238 K . In contrast, the peak intensity of the H–O–H bending mode significantly decreases with decreasing temperature, which, however, also reflects that the spectra of water gradually adopt “ice-like” character upon cooling, as first observed by Zsetsky et al.¹⁶ The temperature-dependent variations in the k spectra systemically propagate into the corresponding n spectra. Here, the amplitude of dispersion in

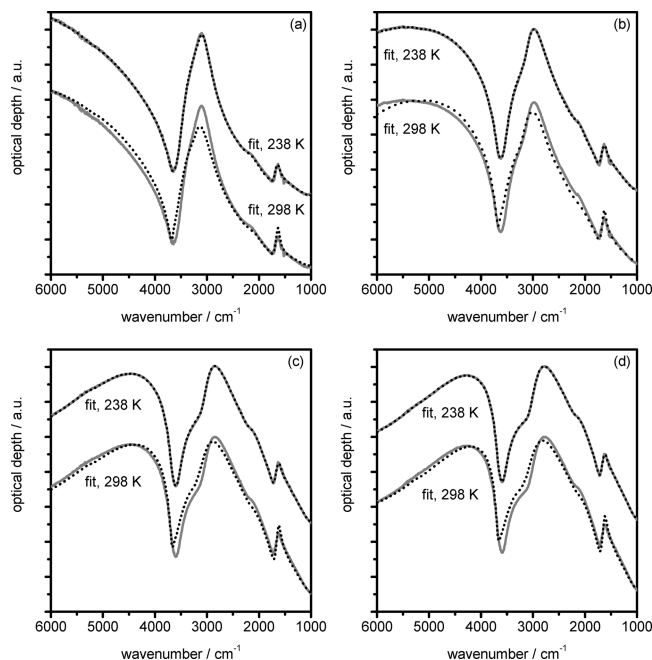


Figure 11. Measured infrared extinction spectra (gray solid lines) of supercooled water droplets at 238 K in comparison with best fit results from Mie calculations (black dotted lines) using (i) the newly derived optical constants of supercooled water at 238 K and (ii) the room-temperature optical constants from Bertie and Lan¹⁴ as input. Measured and calculated spectra corresponding to case study (i) are offset for clarity. The FTIR spectra were recorded during an AIDA expansion experiment with H₂SO₄/H₂O solution droplets as seed aerosol. Retrieved droplet diameters are ranging from 2.2 μm (panel a) to 5.3 μm (panel d).

the O–H stretching regime is increasing with decreasing temperature whereas the opposite trend is apparent in the spectral region of the H–O–H bending mode.

Experimental FTIR extinction spectra of supercooled water droplets from two AIDA expansion experiments at 238 and 252 K and best fit results from Mie calculations using the newly obtained refractive indices as well as the room-temperature optical constants from Bertie and Lan¹⁴ are shown in Figures 11 and 12. As proposed in the preceding section, the near-infrared optical constants of supercooled water from Kou et al.¹¹ were appended to our k spectra at 4500 cm^{-1} , thereby extending the wavenumber regime of the Mie fits to 6000 cm^{-1} .

Note how accurately measured and calculated extinction spectra agree after having optimized the optical constants by the iterative procedure described in the Experimental Section. Again, it is worth emphasizing that our measured droplet spectra, as having been successively recorded during AIDA expansion experiments, cover a broad range of different droplet diameters. That indeed each individual spectrum is well reproduced by the Mie fit therefore underlines the precision of the newly derived low-temperature refractive index data sets for water. In contrast, as already convincingly demonstrated by Zsatsky et al.,^{16,19} the poor quality of the Mie fits with the Bertie and Lan¹⁴ n and k data might intimate the presence of a mixed phase cloud although only supercooled water droplets are present, because adding a suitable volume fraction of ice would reduce the residuals between measured and calculated spectra.

As a final point, we want to compare the cloud droplet diameters that were retrieved from the FTIR spectra analyses with those simultaneously measured with the WELAS optical particle spectrometer for two selected expansion experiments (Figure 13). Remember that the two techniques for deriving the

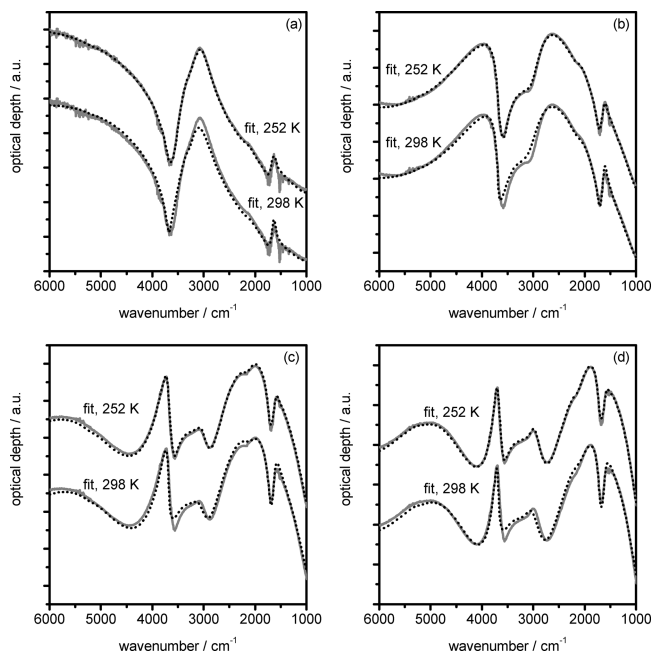


Figure 12. Measured infrared extinction spectra (gray solid lines) of supercooled water droplets at 252 K in comparison with best fit results from Mie calculations (black dotted lines) using (i) the newly derived optical constants of supercooled water at 252 K and (ii) the room-temperature optical constants from Bertie and Lan¹⁴ as input. Measured and calculated spectra corresponding to case study (i) are offset for clarity. The FTIR spectra were recorded during an AIDA expansion experiment with mineral dust particles as seed aerosol. Retrieved droplet diameters are ranging from 2.4 μm (panel a) to 11.1 μm (panel d).

size distribution of the water droplets are fundamentally different. FTIR extinction spectra are recorded in situ in the aerosol vessel (Figure 2), thereby measuring horizontally averaged cloud extinction at medium height of the AIDA chamber. In contrast, the WELAS instrument operates in an ex situ mode, sampling chamber air from a distant point near the bottom of the aerosol vessel. Due to these operational differences, the droplet size distributions measured by WELAS were not directly used as input in our iterative algorithm (eq 5). Instead, the size distribution parameters, initially obtained from Mie fits with the Bertie and Lan¹⁴ optical constants, were iteratively adjusted together with the optical constants in steps (i) and (ii) of our inversion technique. We have, however, checked the consistency of our retrievals with the droplet diameters measured by the WELAS optical particle spectrometer; cf. Figure 13. The temporal evolution of cloud droplet sizes retrieved from the FTIR extinction spectra, using the newly derived low-temperature refractive indices as input, agrees well with the WELAS data, thus validating our strategy to consecutively adjust both the size distribution parameters and the refractive indices. Minor deviations may be due to the different sampling geometries of the two techniques, as outlined above.

After having presented our newly derived n and k spectra, we will now proceed with comparing these data sets to those recently obtained by Zsatsky et al.¹⁹ Three individual n and k data sets from both studies are displayed in the upper panels of Figure 14. In addition, the lowermost panel shows the temperature-induced spectral changes in the O–H stretching regime revealed by the k spectra obtained from our own work and spectra retrieved by Zsatsky et al.¹⁹ In general, both data sets bare the same overall spectral variations in the mid-infrared spectrum of water upon cooling, e.g., the low-frequency shift and intensity increase of the O–H stretching band. The

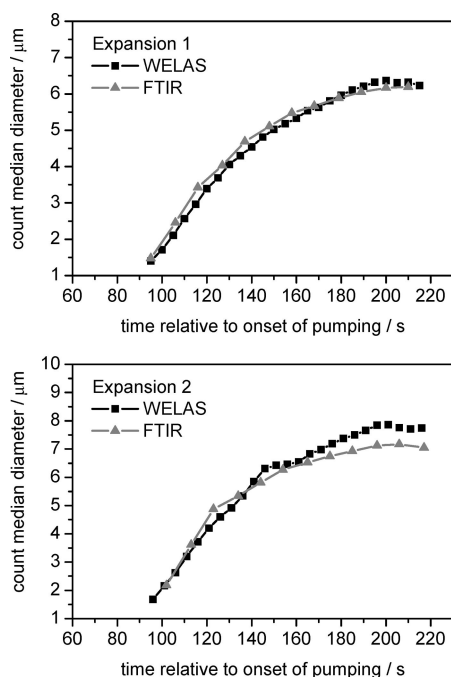


Figure 13. Temporal evolution of count median droplet diameters retrieved from the WELAS and FTIR measurements during two AIDA expansion experiments with supercooled $\text{H}_2\text{SO}_4/\text{H}_2\text{O}$ solution droplets as seed aerosol. Both expansions were started at a mean AIDA gas temperature of about 243 K. The data shown are restricted to the time period before freezing onset of the cloud droplets (see, e.g., Figure 5 for comparison). The FTIR retrievals are based on the newly derived refractive index data set for supercooled water at 238 K. The original WELAS data, comprising about 4000 individual size channels between 0.8 and 45 μm , were fitted by log-normal number distributions of particle sizes.

deviations between the individual n and k spectra are not severe; however, an obviously systematic discrepancy can be made out in the spectra collection. Our own k spectra consistently feature a more intense O–H stretching band whereas the peak intensity in the regime of the H–O–H bending mode is systematically lower than in the data sets obtained by Zsatsky et al.¹⁹ Maximum deviations in the peak intensities of the two absorption bands are in the order of 10%. It appears unlikely that spectral changes of that magnitude are due to the slight differences in temperature between the compared spectra. In addition to these discrepancies in the peak intensities, there are occasionally frequency shifts in the peak position of the O–H stretching band, particularly apparent in the data sets at $T \sim 270$ K shown in the top row of Figure 14. Whereas our own k spectra series exhibits a smooth and continuous low-frequency shift of the O–H stretching mode upon cooling, no such smooth transition occurs from the Bertie and Lan¹⁴ spectrum to the low-temperature data sets of Zsatsky et al.¹⁹ Here, the temperature decrease from 298 to 273 K already leads to a pronounced low-frequency shift of about 50 cm^{-1} , much in contrast to our own study and the earlier results from Pinkley et al.,¹³ as addressed in the introductory section. Further cooling to 240 K then only results in a comparatively small additional band shift of the O–H stretching mode. Zsatsky et al.¹⁹ reported an uncertainty in their refractive index data sets of 4% in the O–H stretching regime. However, error estimation is complicated when an iterative Mie inversion technique is employed to derive the optical constants from measured extinction spectra. The same is true for our own study; we therefore find it problematical to specify such a definite value for the uncertainty of our n and k spectra. Rather, the direct comparison of the results of two

different iterative techniques to derive the refractive indices, as shown in Figure 14, is more illustrative to make clear the magnitude of the uncertainties that can be introduced into the retrieved optical constants. Potential explanations for the small discrepancies between the k spectra obtained in the present study and the data sets from Zsatsky et al.¹⁹ will be discussed in a succeeding paragraph. Via the Kramers–Kronig transformation, these spectral differences in the absorption indices directly propagate into the corresponding n spectra. In addition, the minor offset between the various n spectra at nonabsorbing wavenumbers >4000 cm^{-1} is caused by slightly different values for n at the anchor points used in the subtractive Kramers–Kronig integration.

In Figure 15, we compare the best fit results from Mie calculations using our own as well as the Zsatsky et al.¹⁹ n and k data sets for two selected extinction spectra of supercooled water at 238 and 270 K. Calculated spectra are based on a log-normal number distribution of cloud droplet diameters. The Mie fits with the Zsatsky et al.¹⁹ refractive indices as input also lead to an overall accurate reproduction of our measured infrared spectra, nonetheless revealing slight spectral mismatches that exactly reflect the differences of their optical constants from our own data, as discussed in the previous paragraph. So the extinction maximum at 3000 cm^{-1} is underestimated and, at the same time, the peak intensity at 1600 cm^{-1} slightly overestimated in the Mie calculated spectra for $T = 238$ K. Concerning the fit example at $T = 270$ K, the calculated spectral habitus of the extinction band in the O–H stretching regime is slightly distorted compared to the measured one. The retrieved droplet diameters, however, are virtually unaffected by the choice of the refractive index data sets, i.e., are insensitive to these slight spectral discrepancies.

As a preliminary note to the remaining part of this section, we emphasize the generally good agreement between our and the Zsatsky et al.¹⁹ refractive index data sets. Nevertheless, we consider it worthwhile to focus on the small discrepancies between the various k spectra shown in Figure 14. That two groups employed different Mie inversion techniques to derive the optical constants gives us the unique chance to explicitly assess the inaccuracies which can be associated with these algorithms. To elaborate possible explanations for the spectral deviations, we have to consider four important differences between our iterative approach to derive the optical constants and the strategy employed by Zsatsky et al.¹⁹

(i) As a significant advantage of the Zsatsky et al.¹⁹ study, infrared extinction spectra of the supercooled water droplets were measured down to 460 cm^{-1} , thus including the intermolecular rotational modes of water and ice. Especially in the 800–460 cm^{-1} regime, the variation of the k spectrum with temperature proved to be quite pronounced. Hence, the authors had only to approximate the temperature dependence of the remaining k spectrum <460 cm^{-1} prior to the Kramers–Kronig integration to calculate the corresponding n spectrum. In contrast, as discussed in the Experimental Section, we had to mimic the complete 800–70 cm^{-1} k spectrum by applying a simple mixing rule approach, i.e., approximating the k spectrum as linear superposition of the k spectra from Bertie and Lan¹⁴ and Warren.¹⁵ Inaccuracies in this low-frequency extension will directly infect the n spectrum obtained from the Kramers–Kronig transform but will also propagate into the k spectrum in course of the optimization procedure. But with the Zsatsky et al.¹⁹ k data at hand, we can check our previous error estimation concerning the influence of the 800–70 cm^{-1} extension on the Kramers–Kronig result.

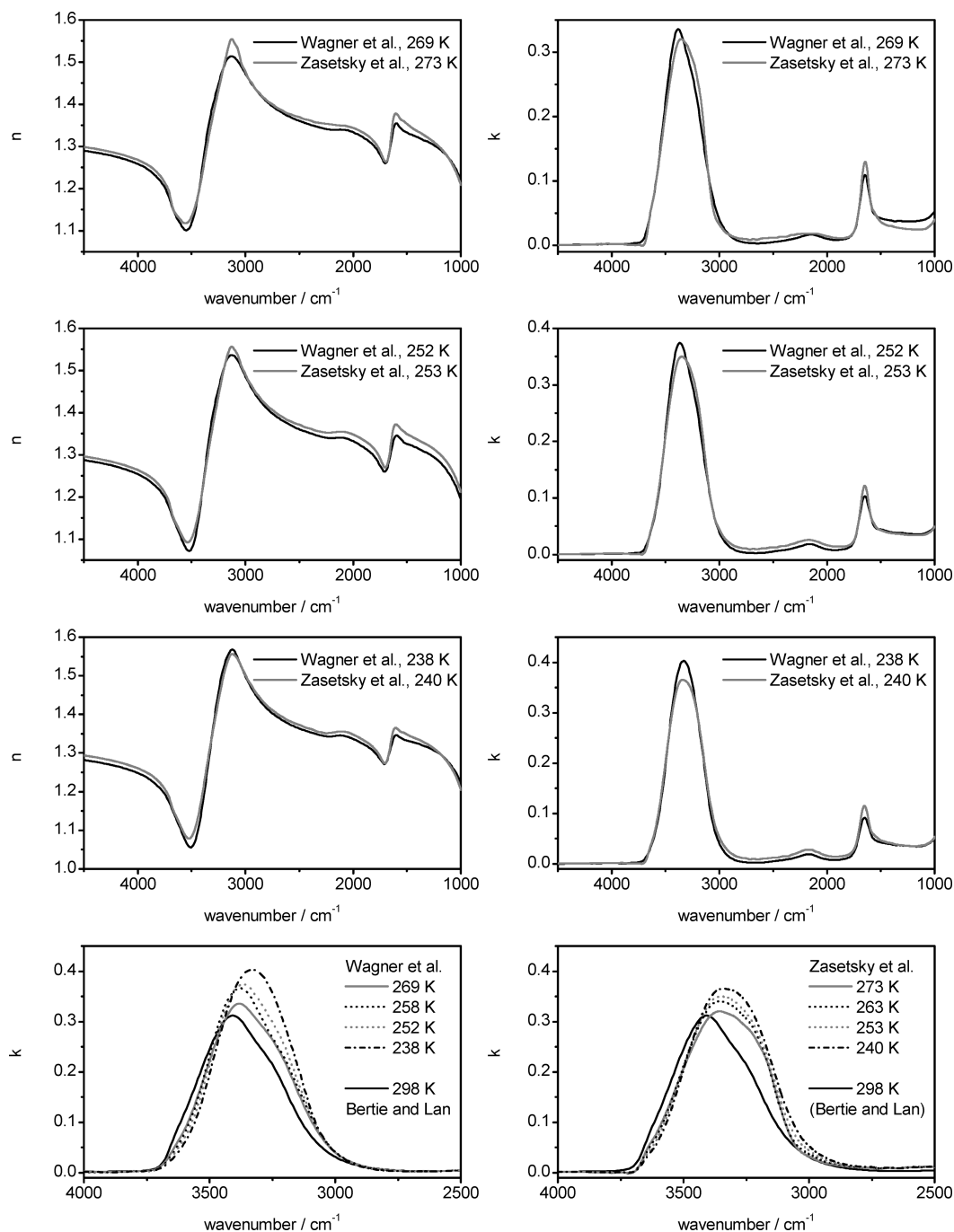


Figure 14. Comparison of the refractive index data sets of supercooled water obtained in the present study with those retrieved by Zasetzky et al.¹⁹ First row: n and k spectra at 269 K (this work) and 273 K (Zasetzky et al.¹⁹). Second row: n and k spectra at 252 K (this work) and 253 K (Zasetzky et al.¹⁹). Third row: n and k spectra at 238 K (this work) and 240 K (Zasetzky et al.¹⁹). The lowermost panels display expanded views of the O–H stretching regime between 4000 and 2500 cm^{-1} for all k spectra obtained in this work (left side) and in the preceding study by Zasetzky et al.¹⁹ (right side). In each case, the room-temperature k spectrum of water from Bertie and Lan¹⁴ is shown for comparison.

Exemplarily, Figure 16 shows again the top panel of Figure 8, i.e., our k spectrum for supercooled water at 252 K with three different low-frequency extensions, but including now the actual k spectrum of supercooled water from 800 to 460 cm^{-1} at 253 K as derived from Zasetzky et al.¹⁹ Obviously, the true k spectrum falls within the error regime covered by the three k spectra calculated using eq 9 with different mixing factors. We therefore conclude that the approximation of the k spectrum of supercooled water at 800–70 cm^{-1} by eq 9 cannot explain the apparent differences between our and the Zasetzky et al.¹⁹ k data sets in the 4500–1100 cm^{-1} regime, as shown in Figure 14. Note again that especially the Kramers–Kronig result for

the 3500–3000 cm^{-1} region is hardly influenced by any variations in the low-frequency k spectra.

(ii) In our present study, we adopted a log-normal number distribution of droplet sizes to fit our measured infrared extinction spectra. In contrast, Zasetzky et al.¹⁹ employed an inversion technique with no functional constraints on the retrieved droplet size distribution (see, e.g., Figure 3 in their publication). We purposely decided to analyze our spectra on the basis of a log-normal distribution because of two reasons. First of all, the droplet size distributions measured with the WELAS instrument indeed quite accurately fitted to log-normal distributions. Second, relaxing the constraints on the droplet size

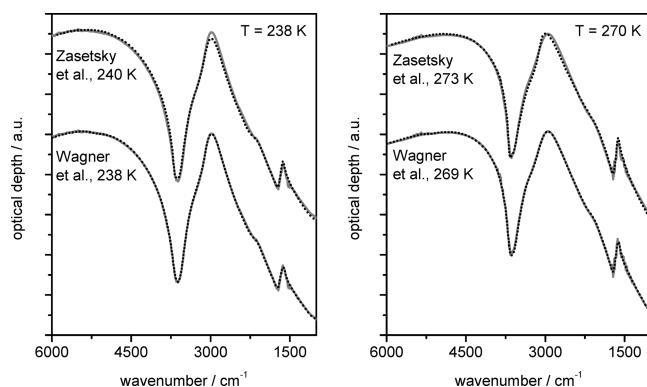


Figure 15. Comparison of the performance of the n and k data sets obtained in the present study with those retrieved by Zasetzky et al.¹⁹ Measured infrared extinction spectra of supercooled water droplets (gray solid lines) at 238 K (left panel) and 270 K (right panel) in comparison with best fit results from Mie calculations, assuming log-normally distributed particle sizes. Left side: Mie fits using the newly derived 238 K as well as the Zasetzky et al.¹⁹ 240 K data sets. Right side: Mie fits using the newly derived 269 K as well as the Zasetzky et al.¹⁹ 273 K data sets. Measured and calculated spectra corresponding to fits with the Zasetzky et al.¹⁹ data sets are offset for clarity. The retrieved count median droplet diameter is insensitive to the choice of the refractive index data set and is about $3.5 \mu\text{m}$ for both fit examples.

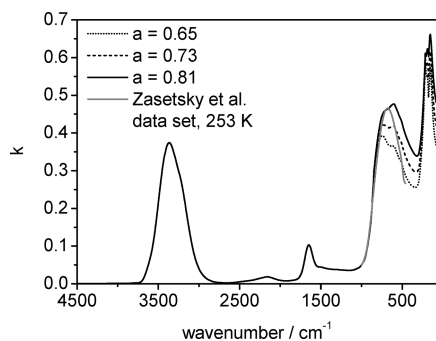


Figure 16. Our newly derived k spectrum for supercooled water at 252 K with three different low-frequency ($800\text{--}70 \text{ cm}^{-1}$) extensions, calculated using eq 9 with mixing factors of $a = 0.65, 0.73,$ and 0.81 (see top panel of Figure 8), in comparison with the actual $1000\text{--}460 \text{ cm}^{-1}$ k spectrum at 253 K as retrieved by Zasetzky et al.¹⁹

distribution might favor the trade off between the retrieved optical constants and the simultaneously retrieved droplet size distribution, now offering an even larger number of independent fitting parameters. To test the influence of different assumptions on the droplet size distribution on the retrieval results, we have repeated the Mie fit shown in the right panel of Figure 15 with the Zasetzky et al.¹⁹ optical constants, now applying an inversion technique with no constraints on the number distribution of the droplet diameters, except for limitation to positive values and application of a weak smoothing function, as described by Arnott et al.³⁸ The best fit results with and without imposing a log-normal constraint on the number distribution of particle sizes are compared in the left panel of Figure 17; the right panel depicts the retrieved volume distributions of droplet diameters.

It becomes evident that the quality of the Mie fit result in the O–H stretching regime can be indeed improved when relaxing the constraints on the droplet size distribution. Figures 15 and 17 illustrate that there is definitely some trade off between the optical constants and the size distribution parameters; i.e., a similar fit result can be obtained when (a) using our 269 K refractive index data set and assuming a log-normal number distribution of particle sizes and (b) using the Zasetzky et al.¹⁹ 273 K data set with no functional constraint on the size distribution. This at least partly accounts for the differences in

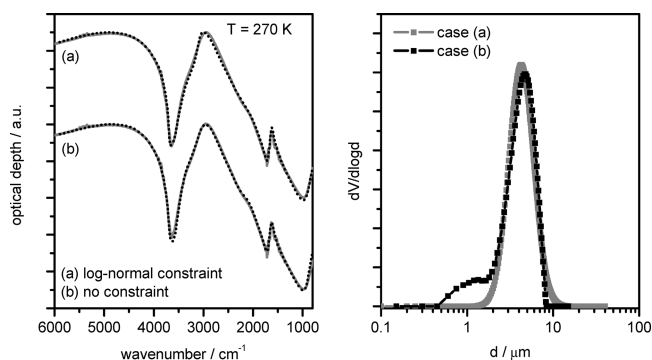


Figure 17. Left panel: Measured infrared extinction spectrum of supercooled water droplets at $T = 270 \text{ K}$ (gray solid lines) in comparison with the best fit results from Mie calculations using the water refractive index data set from Zasetzky et al.¹⁹ (273 K) as input. In (a), shown offset for clarity, a log-normal number distribution of particle sizes was assumed (see right panel of Figure 15). The log-normal constraint was discarded in (b). Retrieved volume distributions of droplet diameters are shown in the right panel.

the refractive index data sets obtained in the present study and those deduced by Zasetzky et al.¹⁹ (Figure 14, top row, right panel), showing 5% deviation in the peak intensity of the O–H stretching band as well as a frequency shift of about 25 cm^{-1} in the peak position of this absorption band. In the specific example shown in Figure 17, a significant volume fraction of smaller droplets has to be included to improve the performance of the Mie fit with the Zasetzky et al.¹⁹ n and k data set. Note that the small droplet mode ($d \sim 1 \mu\text{m}$) is even more dominant in the corresponding number distribution of droplet diameters. Our simultaneous measurements with the WELAS optical particle spectrometer, however, do not support such a pronounced bimodal number distribution of particle sizes. We therefore favor our approach of minimizing the number of independent fitting parameters by imposing a log-normal size distribution on our retrieval procedure.

(iii) The analysis of the preceding paragraph has clearly demonstrated that the trade off between the optical constants and the simultaneously retrieved size distribution parameters may be a crucial issue in the retrieval algorithm. Therefore, as already highlighted in the Experimental Section, a series of extinction spectra corresponding to largely varying droplet diameters was employed as basis for the derivation of optical constants for supercooled water to improve the uniqueness of the retrieval results. Minimum droplet diameters were usually in the order of $2 \mu\text{m}$; maximum droplet diameters, depending on temperature (i.e., the available water vapor concentration) and seed aerosol number concentration, were about $6 \mu\text{m}$ for the 238 and 269 K expansion experiments, and about $11 \mu\text{m}$ for the spectra series recorded at 252 and 258 K (i.e., the collection of spectra monitored at $T = 256$ and 260 K). Also Zasetzky et al.¹⁹ used a series of infrared spectra of differently sized water droplets as input for their retrieval approach, however, usually spanning only the $1\text{--}4 \mu\text{m}$ diameter range. For larger cloud droplets, whose infrared spectra are increasingly dominated by light scattering, they reported problems to achieve stable solutions for the retrieval results. As described in the Experimental Section, we encountered the same problem when trying to derive a water refractive index set in the $265\text{--}270 \text{ K}$ temperature range from expansion experiments with low number concentrations of mineral dust particles as seed aerosol, where the generated cloud droplets rapidly grew to diameters $> 10 \mu\text{m}$. However, our algorithm provided stable results when applied to a spectra series including at least two spectra with droplet diameters $< 6 \mu\text{m}$. This slightly improved performance compared

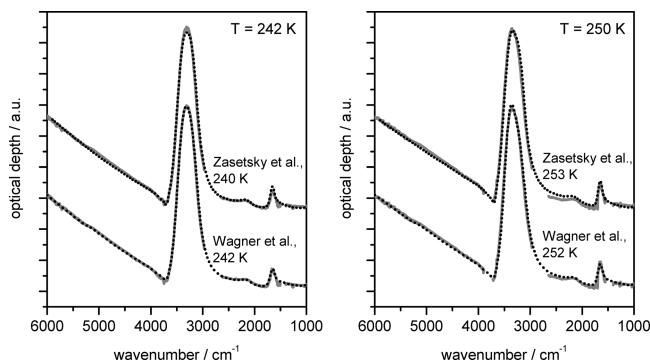


Figure 18. Measured infrared extinction spectra of supercooled water clouds (gray solid lines) made by activating SOA particles at 242 K (left panel) and 250 K (right panel) in comparison with best fit results from Mie calculations (dotted lines), assuming log-normally distributed cloud droplet sizes. Left side: Mie fits using the newly derived 242 K data set (linear interpolation between our 238 and 252 K data sets) as well as the Zasetsky et al.¹⁹ data set for 240 K. Right side: Mie fits using the newly derived 252 K as well as the Zasetsky et al.¹⁹ 253 K data sets. Measured and calculated spectra corresponding to fits with the Zasetsky et al.¹⁹ data sets are offset for clarity. Spectral regions contaminated by strong infrared absorption bands of cyclohexane (which had been added to scavenge OH radicals from the ozonolysis of α -pinene) are omitted in the recorded spectra. The good agreement between measured and calculated spectra indicates that the residual organic matter inside the cloud droplets does not alter the water extinction features.

to the Zasetsky et al.¹⁹ approach might be attributed to the reduced number of independent fitting parameters by using the log-normal distribution to represent the cloud droplet size distribution. Nevertheless, one might argue that the different size ranges of the water droplets, whose infrared spectra were included in the retrieval algorithms, might explain the discrepancies between the two refractive index data sets (Figure 14). Specifically, one might criticize that our infrared spectra are usually more dominated by light scattering than the spectra recorded by Zasetsky et al.,¹⁹ thereby being less sensitive to small changes in the spectrum of the absorption index. Very recent AIDA expansion experiments, however, give us the chance to check whether our newly derived refractive index data sets are also appropriate to accurately reproduce the extinction spectra of very small cloud droplets with $d < 1 \mu\text{m}$. These experiments were dedicated to determine the temperature dependence of the yield of secondary organic aerosol (SOA) from the ozonolysis of monoterpenes as well as to test the ability of the organic aerosol to act as nuclei for cloud formation (droplets and/or ice crystals) in the 253–238 K temperature range. SOA particles (CMD $\sim 300 \text{ nm}$, $N \sim 40\,000 \text{ cm}^{-3}$) were generated by the controlled, stepwise oxidation of α -pinene with an excess of ozone. After the depletion of α -pinene and the determination of the aerosol yields, standard AIDA expansion experiments were started as described in the Experimental Section. Note that despite the significant SOA mass concentration, absorption features of the organic matter were not detected in the reference spectra recorded before the start of the expansions. Two selected FTIR extinction spectra recorded during expansion experiments at $T = 242$ and 250 K are shown in Figure 18. These expansions only resulted in cloud droplet activation of the SOA particles; i.e., droplet freezing did not occur. Due to the high SOA number concentration, the water extinction spectra are only slightly distorted by light scattering as the cloud droplets did not grow to sizes larger than $1 \mu\text{m}$ in diameter. Measured spectra are compared to the best fit results from Mie calculations with our own and the Zasetsky et al.¹⁹ refractive index data sets. To obtain a refractive index data set

for $T = 242 \text{ K}$, we linearly interpolated between our k spectra retrieved at 238 and 252 K and performed the Kramers–Kronig integration to attain the corresponding n spectrum. Note how precisely also extinction spectra of submicron water droplets are mimicked in Mie calculations with our new refractive index data sets as input. This underlines that our Mie inversion technique yields consistent retrieval results for the refractive indices, although only relying on infrared spectra of larger ($d > 2 \mu\text{m}$) water droplets.

(iv) Finally, we want to take a closer look at the different methodologies used to optimize the complex refractive indices of supercooled water. In both our and the Zasetsky et al.¹⁹ study, the room-temperature k spectrum from Bertie and Lan¹⁴ was used as the starting point for the retrieval procedure. In the course of the optimization processes, this spectrum was iteratively adjusted by minimizing the residua between observed and calculated extinction spectra. In our own approach, all data points of the k spectrum were used as independent optimization parameters. As the only functional constraint on the retrieved k spectra, a weak smoothing function was applied to avoid the appearance of unphysical spikes in the data sets. On the contrary, the inversion technique applied by Zasetsky et al.,¹⁹ consisting of an inner and outer iteration loop, involves two explicit mathematical expressions to adjust the Bertie and Lan¹⁴ k spectrum. In the inner loop, the k spectrum is linearly scaled by a frequency-independent scaling coefficient k' . This approach was adopted from an algorithm originally presented by Clapp et al.³ to retrieve the low-temperature optical constants of ice from measured infrared extinction spectra. Here, the coefficient k' was introduced when a first guess for the k spectrum of ice was derived from a nonscattering aerosol extinction spectrum. The scaling factor k' simply accounts for the fact that the exact number and volume concentrations of the ice particles were unknown. But note that transferring this approach to adjust the k spectrum of water might be dangerous, because k' will equally scale both the magnitude of the absorption bands in the O–H stretching and H–O–H bending regime. However, upon cooling, the intensities of these water absorption bands evolve in the opposite direction, the O–H stretching mode becoming more intense and the H–O–H bending mode becoming less intense. It appears possible that the implementation of k' leads to the small systematic deviations of the Zasetsky et al.¹⁹ k data sets from our own results, i.e., may explain the different intensities in the two water absorption bands (see Figure 14). In the outer iteration loop of the Zasetsky et al.¹⁹ approach, the k spectra are fine-tuned by applying a mathematical correction originally adopted by Clapp et al.³ and explicitly derived in the work by Dohm et al.³⁰ (eq 12 therein). Clapp et al.³ had to correct their first guess k spectrum, obtained from the nonscattering extinction spectrum of ice crystals, because the absorption spectrum of particles is different from that of the corresponding bulk sample, i.e., is not directly proportional to the imaginary index k (cf. eq 2). Hence, the difference between observed and calculated extinction spectra of larger ice crystals was used to adjust the initial guess k spectrum. However, it is not intuitively evident why the same mathematical correction should properly correct for the spectral inaccuracies introduced in the inner loop of the Zasetsky et al.¹⁹ approach by using a frequency-independent scaling factor k' to adjust the k spectrum of water. These procedural differences in extracting the optical constants of supercooled water from the recorded extinction spectra most likely explain the small differences between the various refractive index data sets, as shown in Figure 14.

Summary

During expansion experiments at the AIDA aerosol chamber facility, an extensive collection of mid-infrared extinction spectra of micron-sized supercooled water droplets was recorded. Dry mineral dust particles, leaf surface bacteria from dispersion of a bacterial suspension, and supercooled sulfuric acid solution droplets were used as seed aerosol particles to study cloud formation at temperatures between 270 and 236 K. Applying a Mie inversion technique, we retrieved four data sets of complex refractive indices for supercooled water at 269, 258, 252, and 238 K in the 4500 to 1100 cm^{-1} wavenumber range from the measured spectra series. The new data sets reveal pronounced temperature-dependent spectral variations in the water spectrum, e.g., an increase of 30% in the intensity of O–H stretching mode upon cooling from 298 to 238 K, accompanied by a low-frequency band shift of about 70 cm^{-1} . With the new low-temperature optical constants as input data in Mie calculations, excellent agreement between measured and calculated infrared extinction spectra was observed for a broad range of different particle sizes, extending from submicron droplets to water droplets $>10 \mu\text{m}$ in diameter. The performance of the new n and k data sets was further tested by comparing retrieved droplet diameters with those independently measured with an optical particle spectrometer.

With decreasing temperature, the liquid water spectral habitus gradually approaches the spectral characteristics of ice. The linear combination of the refractive indices of room-temperature water and ice only roughly accounts for the observed spectral trends. The new refractive index data will therefore significantly improve the accuracy by which the ratio of supercooled water droplets to ice crystals in mixed phase clouds can be retrieved, not only in future laboratory experiments at the AIDA chamber but also in mid-infrared remote sensing applications. The deduced low-temperature optical constants of water proved to be in good agreement with the data sets recently published by Zsazskey et al.¹⁹ Nevertheless, a detailed analysis of small spectral deviations between the various data sets sheds some light on inaccuracies which might be introduced into the retrieved optical constants when using different iterative inversion techniques.

Acknowledgment. We are grateful for the continuous support by all members of the AIDA staff. We thank Paul Connolly for his analysis of the CPI measurements. The work has been funded by the Helmholtz-Gemeinschaft Deutscher Forschungszentren as part of the program “Atmosphere and Climate”.

Supporting Information Available: Text files of complex refractive indices of supercooled water from 4500 to 1100 cm^{-1} at $T = 269, 258, 252,$ and 238 K . This material is available free of charge via the Internet at <http://pubs.acs.org>.

References and Notes

- (1) Massie, S. T.; Goldman, A. *J. Quant. Spectrosc. Radiat. Transfer* **2003**, *82*, 413.
- (2) Rothman, L. S.; Barbe, A.; Benner, D. C.; Brown, L. R.; Camy-Peyret, C.; Carleer, M. R.; Chance, K.; Clerbaux, C.; Dana, V.; Devi, V. M.; Fayt, A.; Flaud, J. M.; Gamache, R. R.; Goldman, A.; Jacquemart, D.;

- Jucks, K. W.; Lafferty, W. J.; Mandin, J. Y.; Massie, S. T.; Nemtchinov, V.; Newnham, D. A.; Perrin, A.; Rinsland, C. P.; Schroeder, J.; Smith, K. M.; Smith, M. A. H.; Tang, K.; Toth, R. A.; Vander Auwera, J.; Varanasi, P.; Yoshino, K. *J. Quant. Spectrosc. Radiat. Transfer* **2003**, *82*, 5.
- (3) Clapp, M. L.; Miller, R. E.; Worsnop, D. R. *J. Phys. Chem.* **1995**, *99*, 6317.
- (4) Niedziela, R. F.; Norman, M. L.; DeForest, C. L.; Miller, R. E.; Worsnop, D. R. *J. Phys. Chem. A* **1999**, *103*, 8030.
- (5) Norman, M. L.; Qian, J.; Miller, R. E.; Worsnop, D. R. *J. Geophys. Res. (Atmos.)* **1999**, *104*, 30571.
- (6) Norman, M. L.; Miller, R. E.; Worsnop, D. R. *J. Phys. Chem. A* **2002**, *106*, 6075.
- (7) Tisdale, R. T.; Glandorf, D. L.; Tolbert, M. A.; Toon, O. B. *J. Geophys. Res. (Atmos.)* **1998**, *103*, 25353.
- (8) Biermann, U. M.; Luo, B. P.; Peter, T. *J. Phys. Chem. A* **2000**, *104*, 783.
- (9) Myhre, C. E. L.; Christensen, D. H.; Nicolaisen, F. M.; Nielsen, C. J. *J. Phys. Chem. A* **2003**, *107*, 1979.
- (10) Myhre, C. E. L.; Grothe, H.; Gola, A. A.; Nielsen, C. J., Optical constants of $\text{HNO}_3/\text{H}_2\text{O}$ and $\text{H}_2\text{SO}_4/\text{HNO}_3/\text{H}_2\text{O}$ at low temperatures in the infrared region. *J. Phys. Chem. A*, in press.
- (11) Kou, L. H.; Labrie, D.; Chylek, P. *Appl. Opt.* **1993**, *32*, 3531.
- (12) Zsazskey, H. R. *J. Mol. Struct.* **1995**, *350*, 95.
- (13) Pinkley, L. W.; Sethna, P. P.; Williams, D. J. *Opt. Soc. Am.* **1977**, *67*, 494.
- (14) Bertie, J. E.; Lan, Z. D. *Appl. Spectrosc.* **1996**, *50*, 1047.
- (15) Warren, S. G. *Appl. Opt.* **1984**, *23*, 1206.
- (16) Zsazskey, A. Y.; Khalizov, A. F.; Sloan, J. J. *J. Chem. Phys.* **2004**, *121*, 6941.
- (17) Yang, P.; Wei, H. L.; Baum, B. A.; Huang, H. L.; Heymsfield, A. J.; Hu, Y. X.; Gao, B. C.; Turner, D. D. *J. Quant. Spectrosc. Radiat. Transfer* **2003**, *79*, 1171.
- (18) King, M. D.; Platnick, S.; Yang, P.; Arnold, G. T.; Gray, M. A.; Riedi, J. C.; Ackerman, S. A.; Liou, K. N. *J. Atmos. Ocean. Technol.* **2004**, *21*, 857.
- (19) Zsazskey, A. Y.; Khalizov, A. F.; Earle, M. E.; Sloan, J. J. *J. Phys. Chem. A* **2005**, *109*, 2760.
- (20) Möhler, O.; Büttner, S.; Linke, C.; Schnaiter, M.; Saathoff, H.; Stetzer, O.; Wagner, R.; Krämer, M.; Mangold, A.; Ebert, V.; Schurath, U., Effect of Sulphuric Acid Coating on Heterogeneous Ice Nucleation by Soot Aerosol Particles. *J. Geophys. Res.* **2005**, *110*, D11210.
- (21) Möhler, O.; Stetzer, O.; Schaeffers, S.; Linke, C.; Schnaiter, M.; Tiede, R.; Saathoff, H.; Krämer, M.; Mangold, A.; Budz, P.; Zink, P.; Schreiner, J.; Mauersberger, K.; Haag, W.; Kärcher, B.; Schurath, U. *Atmos. Chem. Phys.* **2003**, *3*, 211.
- (22) Lawson, R. P.; Baker, B. A.; Schmitt, C. G.; Jensen, T. L. *J. Geophys. Res. (Atmos.)* **2001**, *106*, 14989.
- (23) Möhler, O.; Linke, C.; Saathoff, H.; Schnaiter, M.; Wagner, R.; Schurath, U. Ice nucleation on flame soot aerosol of different organic carbon content. *Meteorol. Z.*, in press.
- (24) Bohren, C. F.; Huffman, D. R. *Absorption and Scattering of Light by Small Particles*; John Wiley & Sons: New York, 1983.
- (25) Arnott, W. P.; Dong, Y. Y.; Hallett, J. *Appl. Opt.* **1995**, *34*, 541.
- (26) Hawranek, J. P.; Neelakantan, P.; Young, R. P.; Jones, R. N. *Spectrochim. Acta, Part A* **1976**, *32*, 75.
- (27) Rouleau, F.; Martin, P. G. *Astrophys. J.* **1991**, *377*, 526.
- (28) Milham, M. E.; Frickel, R. H.; Embury, J. F.; Anderson, D. H. *J. Opt. Soc. Am.* **1981**, *71*, 1099.
- (29) Signorelli, R.; Luckhaus, D. *J. Phys. Chem. A* **2002**, *106*, 4855.
- (30) Dohm, M. T.; Potschavage, A. M.; Niedziela, R. F. *J. Phys. Chem. A* **2004**, *108*, 5365.
- (31) Wagner, R.; Mangold, A.; Möhler, O.; Saathoff, H.; Schnaiter, M.; Schurath, U. *Atmos. Chem. Phys.* **2003**, *3*, 1147.
- (32) Wagner, R.; Möhler, O.; Saathoff, H.; Stetzer, O.; Schurath, U. *J. Phys. Chem. A* **2005**, *109*, 2572.
- (33) Press, W. H.; Teukolsky, S. A.; Vetterling, W. T.; Flannery, B. P. *Numerical Recipes in C: The Art of Scientific Computing*; Cambridge University Press: Cambridge, U.K., 1992.
- (34) Ahrenkiel, R. K. *J. Opt. Soc. Am.* **1971**, *61*, 1651.
- (35) Hawranek, J. P.; Neelakantan, P.; Young, R. P.; Jones, R. N. *Spectrochim. Acta, Part A* **1976**, *32*, 85.
- (36) Ohta, K.; Ishida, H. *Appl. Spectrosc.* **1988**, *42*, 952.
- (37) Hare, D. E.; Sorensen, C. M. *J. Chem. Phys.* **1987**, *87*, 4840.
- (38) Arnott, W. P.; Schmitt, C.; Liu, Y. G.; Hallett, J. *Appl. Opt.* **1997**, *36*, 5205.